Research Square

Preprints are preliminary reports that have not undergone peer review.
They should not be considered conclusive, used to inform clinical practice,
or referenced by the media as validated information.

DEM-FF: A Universal Machine Learning Force Field for Earth's Interior Studies

Xiancai Lu

xcljun@nju.edu.cn

Nanjing University https://orcid.org/0000-0001-8977-2661

Kai Wang

https://orcid.org/0000-0003-3621-5524

Yichu Zhang

Nanjing University

Article

Keywords: machine-learning force field (MLFF), Earth's interior, free-energy calculation, core-mantle differentiation, hydrogen partitioning

Posted Date: June 16th, 2026

DOI: https://doi.org/10.21203/rs.3.rs-9140615/v1

License: This work is licensed under a Creative Commons Attribution 4.0 International License.
Read Full License

Additional Declarations: There is **NO** Competing Interest.

DEM-FF: A Universal Machine Learning Force Field for Earth's Interior Studies

Kai Wang, Yichu Zhang, Xiancai Lu*

Affiliation:

State Key Laboratory of Critical Earth Material Cycling and Mineral Deposits, Frontier Science Center for Critical Earth Material Cycle, School of Earth Sciences and Engineering, Nanjing University, Nanjing, Jiangsu 210023, China

*Correspondence and requests for materials should be addressed to Xiancai Lu (xcljun@nju.edu.cn).

Abstract

Universal machine-learning force fields (uMLFFs) have transformed computational materials science by allowing rapid material discovery across broad chemical spaces. Planetary material simulations, however, present challenges beyond the capability of current uMLFF. The extreme pressures, high temperatures, and chemically complex multi-component system of Earth's deep interior lie far outside their training dataset. Moreover, many fundamental questions in deep-Earth geochemistry rely on accurate free-energy calculations via thermodynamic integration (TI), and no existing uMLFF supports such calculations. Here we introduce DEM-FF (Deep-Earth Materials Force Field), a universal MLFF that overcomes both barriers. DEM-FF covers 25 elements within major geological systems, including fluids, volatiles, silicate melts, minerals, and metallic alloys, and maintains DFT-level accuracy from 0 to 360 GPa and 300 to 10,000 K, with energy RMSE below 10 meV/atom and force RMSE below 0.3 eV/Å. Crucially, configurations sampled along complete TI pathways are incorporated during training, providing DEM-FF the ability to perform reliable free-energy calculations. We validate this by reproducing experimentally measured water solubilities in basaltic melts at 0.1 to 0.5 GPa. We then apply DEM-FF to investigate hydrogen partitioning between pyrolitic silicate melt and liquid iron alloy during core formation using two-phase coexistence simulations with self-consistent redox control. These simulations reveal that compositionally realistic systems yield partition coefficients orders of magnitude lower than those from simplified binary models, and constrain Earth's core hydrogen content to approximately 560-840 ppm. This value is substantially below previous estimates and implies that hydrogen alone cannot account for the core's density deficit. DEM-FF provides a unified framework for compositionally realistic simulations of core-mantle differentiation, volatile cycling, and high-pressure material behaviors across Earth's interior.

Keywords: machine-learning force field (MLFF); Earth's interior; free-energy calculation; core-mantle differentiation; hydrogen partitioning

Introduction

Machine-learning force fields (MLFFs) have greatly expanded the scope of atomistic simulations by delivering DFT-comparable accuracy while extending accessible system sizes and timescales far beyond first-principles methods[1–5]. In deep-Earth science, MLFFs have been applied to a range of studies including thermal transport in mantle minerals[6,7], volatile behaviors in silicate melts[8,9], the roles of light elements in the core[10,11], and mineral phase transitions under extreme conditions[12]. Building an MLFF, however, still demands extensive first-principles data generation, repeated model optimization, and careful validation. These steps carry substantial computational costs and require significant domain expertise. To remove these barriers, the materials-science community has developed universal MLFFs (uMLFFs). Trained on millions of diverse atomic configurations, models such as M3GNet[13], CHGNet[14], MACE-MP-0[15], ORB[16], GPTFF[17], MatterSim[18], and DPA-2[19] aim to generalize across broad chemistries and have been used to accelerate computational materials discovery. These models, however, are overwhelmingly trained on crystalline or near-equilibrium structures at moderate pressures and temperatures from materials-science databases (e.g., the Materials Project[20]). By contrast, the atomic environments encountered in deep-Earth interiors differ fundamentally from those databases, where it involves highly disordered liquids and melts, extreme compression, and chemically complex multicomponent systems across wide *P*-*T* ranges. When standard uMLFFs are directly extrapolated to mantle or core conditions (for example, silicate melts above 3000 K and 20 GPa), they often produce numerical instability or even unphysical results. Another limitation of current MLFFs concerns free-energy calculations via thermodynamic integration (TI). TI requires a force field that remains stable along unphysical alchemical pathways parameterized by a coupling parameter λ that connects a reference system ($\lambda = 0$) to the fully interacting system ($\lambda = 1$)[21]. Because MLFFs are trained exclusively on physical configurations ($\lambda = 1$), they typically fail to describe the intermediate states ($0 < \lambda < 1$) needed for the free-energy computations that are essential for determining phase stabilities and element partitioning[22–26].

To address these challenges, we present DEM-FF (Deep-Earth Materials Force Field),

a universal MLFF designed for simulating Earth and planetary interiors. A reliable model for this domain must handle diverse chemical environments (melts, fluids, minerals, solid-solutions, and multi-component mixtures), maintain accuracy across extreme *P-T* conditions, and remain stable along the full TI pathways needed for free-energy calculations. DEM-FF is constructed through an integrated strategy that explicitly and systematically samples the pressure-temperature-composition-λ (*P-T-X-*λ) space characteristic of planetary interiors. The model covers 25 elements that represent Earth's major compositional reservoirs: core-forming metals (Fe, Ni), silicate components of the crust and mantle (Mg, Ca, Al, Na, K, Mn, Ti, W, B, P, Si, O), volatile species (H, C, N, S, F, Cl, He, Ne, Ar, Kr, Xe), and their mutual interactions. It is applicable from ambient pressure to 360 GPa and from 300 K to over 10,000 K. Based on an E(3)-equivariant MACE-LES architecture[27,28] and trained on a comprehensive DFT dataset, DEM-FF achieves force and energy accuracies comparable to specialized, system-specific MLFFs. We demonstrate DEM-FF's performance through two demanding applications. First, we carry out absolute free-energy calculations to determine the water solubility in basaltic melts. This benchmark confirms that DEM-FF remains stable along non-physical TI pathways and yields solubilities in quantitative agreement with experiments. Second, we conduct two-phase direct coexistence simulations to investigate hydrogen partitioning between silicate melts and liquid iron under self-consistent redox conditions. By explicitly treating realistic multicomponent chemistry and variable oxygen fugacity, we reveale substantial deviations from predictions based on simplified systems. These deviations lead us to reassess hydrogen distribution during core-mantle differentiation and to revise estimates of Earth's primordial hydrogen budget. Together, these results show that DEM-FF can serve as a unified foundation for simulation of compositionally realistic problems in Earth's interior.

Training strategy of DEM-FF

The training strategy of DEM-FF was designed to comprehensively cover the complex chemical and thermodynamic space relevant to Earth's interior (Fig. 1). We constructed

an initial training dataset covering 25 elements and five material classes that represent Earth's major reservoirs: (1) volatile-bearing fluids; (2) silicate melts with variable compositions and volatile contents; (3) major minerals from the upper mantle, transition zone, and lower mantle; (4) solid and liquid iron alloys; and (5) artificially constructed multicomponent systems designed to improve the model's generalization capability. To support accurate free-energy calculations, the training dataset also explicitly includes structures sampled at multiple λ values along TI pathways (Methods). A central challenge in constructing DEM-FF is the enormous high-dimensional parameter space. If we discretized pressure into 36 states (0-360 GPa at 10 GPa intervals), temperature into 20 states (300-10,000 K at 500 K intervals), the λ parameter into 11 values (λ = 0.0-1.0 at 0.1 intervals), and considering ~10^4 distinct chemical compositions (Methods), these would yield a combinatorial space exceeding ~ 10^7 state points, each requiring first-principles calculations for adequate sampling. Brute-force enumeration of this space would be computationally prohibitive.

To overcome this dimension explosion, we employed an active-learning framework that concentrates computational effort on the most informative atomic configurations. The framework builds on the DP-GEN protocol[29] with several modifications described below. In each iteration, an ensemble of independently trained models drove exploratory molecular dynamics simulations across the target *P*-*T*-*X*-λ regime. On-the-fly chemical perturbations, including elemental substitutions, insertions, and removals, were applied during these simulations to push the system into new chemical environments. Configurations with high predictive variance among the ensemble models were flagged as uncertain candidates for DFT labeling. In a typical iteration, the number of such uncertain configurations can reach 10^5 configurations. However, because MD trajectories are inherently correlated in time, consecutive frames near an uncertain region tend to be structurally very similar to one another and carry little additional information. To eliminate this redundancy, we applied a diversity-aware selection procedure[30] based on principal component analysis (PCA) of the MACE atomic descriptors followed by farthest-point sampling (FPS), which retains a structurally diverse subset of configurations. The selected structures were recomputed

with DFT to obtain accurate energies, forces, and stresses, and incorporated into the training set for the next iteration.

After 12 active-learning iterations, convergence was reached with over 30,000 configurations, a dataset comparable in size to what is typically required for a single system-specific MLFF, yet covering a *P-T-X-λ* parameter space orders of magnitude larger. Three innovations in the training strategy make this possible. First, on-the-fly chemical perturbations enable efficient exploration of the high-dimensional compositional space by generating chemically diverse configurations within each simulation trajectory, rather than relying on pre-defined compositions alone. Second, the explicit inclusion of λ-intermediate configurations ($0 < \lambda < 1$) in the training data provides DEM-FF with the capability for free-energy calculations, which is absent from all current uMLFFs. Meanwhile, it also allows DEM-FF to explore unphysical atomic configurations that are far from equilibrium states and substantially improves the robustness of DEM-FF across diverse and extreme conditions. Finally, diversity-aware selection via PCA and FPS massively reduces the number of DFT calculations per iteration by nearly two orders of magnitude, which makes the iterative workflow computationally tractable.

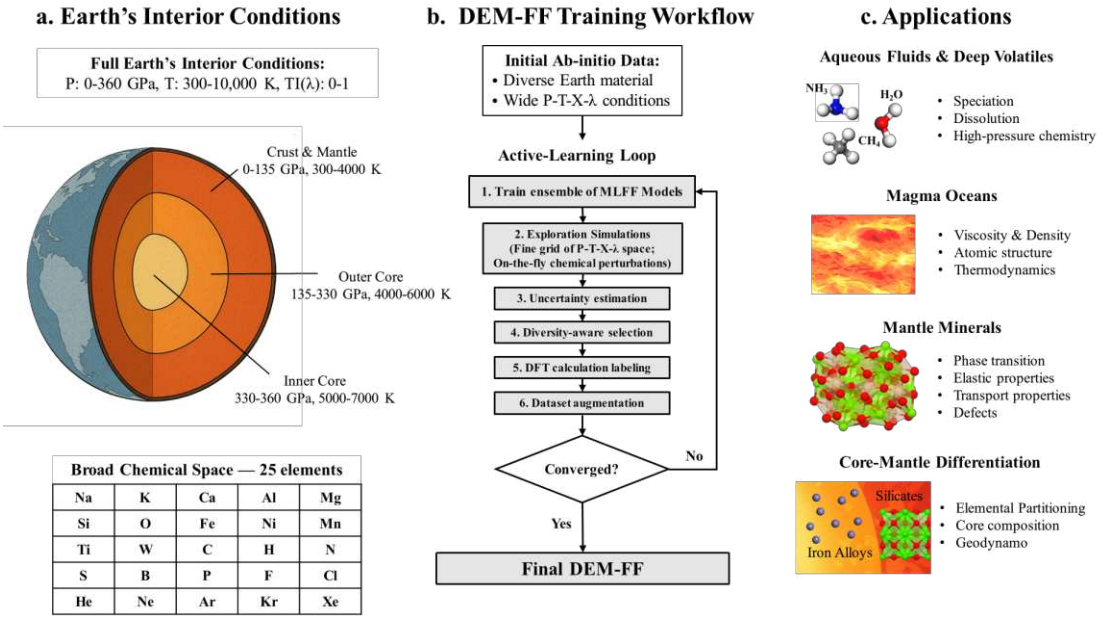


Fig. 1 | Construction workflow and target applications of DEM-FF.

a, DEM-FF is designed to cover the full range of Earth's interior conditions (0-360GPa,

300-10000 K). The model spans a broad chemical space of 25 elements including major rock-forming components, core-forming metals, volatiles, and noble gases, and explicitly includes thermodynamic integration coupling states (λ = 0-1). b, The active-learning workflow begins with an initial *ab-initio* dataset of diverse deep-Earth materials sampled across wide *P-T-X-*λ conditions. An iterative loop then refines the model through six steps: (1) training an ensemble of independent MLFF models; (2) running exploratory molecular dynamics simulations over a dense *P-T-X-*λ grid with on-the-fly chemical perturbations (elemental substitutions, insertions, and removals); (3) quantifying prediction uncertainty via ensemble variance; (4) selecting structurally diverse candidates through PCA-based farthest-point sampling; (5) labeling selected configurations with DFT calculations; and (6) augmenting the training dataset. The loop terminates once model performance converges, yielding the final DEM-FF. c, Representative applications enabled by DEM-FF, including speciation and dissolution of aqueous fluids and deep volatiles; viscosity, density, and thermodynamic properties of magma oceans; phase transitions, elasticity, transport properties, and defect chemistry of mantle minerals; and elemental partitioning, core composition, and geodynamo processes during or after core-mantle differentiation.

Results

Validation across Earth's interior

To systematically evaluate DEM-FF across the full range of Earth's interior, we selected five validation systems that represent geochemical environments from the crust to the inner core: (1) an aqueous fluid at crustal conditions (1 GPa, 1200 K), representing shallow hydrothermal environments; (2) a deep volatile H_2O-CO_2 fluid at mid-mantle pressures (50 GPa, 3000 K); (3) a pyrolite melt at deep magma-ocean conditions (100 GPa, 5000 K); (4) an Fe-bearing bridgmanite crystal at lower-mantle conditions (135 GPa, 5000 K), the most abundant mineral in Earth's interior; and (5) a liquid iron alloy at inner-core conditions (360 GPa, 6000 K), representing the metallic core. None of these configurations were explicitly included in the training dataset. DEM-FF accurately reproduces DFT energies, forces, and stresses of all the five systems (Fig. 2).

The force root-mean-square error (RMSE) remains below 0.3 eV/Å, the energy RMSE below 10 meV/atom, and the stress RMSE below 1.41 GPa. These error levels are comparable to those reported for system- specific MLFFs[8,31].

Beyond these five representative systems, we further validated DEM-FF against 553 inorganic crystalline compounds from the Inorganic Crystal Structure Database (ICSD) [32]. The model accurately reproduced the lattice parameters of a wide range of chemically and structurally complex crystals (Extended Data Fig. 1). DEM-FF also reproduces the pressure-induced phase transitions of major Mg-Si-O mantle minerals, in excellent agreement with DFT calculations (Extended Data Fig. 2). We further tested whether DEM-FF can capture subtle electronic temperature (T_{el}) effects in DFT calculations. The T_{el} in finite-temperature DFT controls the electronic entropy contribution to the total free energy and measurably influences properties such as phase stability and melting at high pressures[33–36]. We treated T_{el} as an additional parameter in the training data and verified that DEM-FF responds sensitively to this effect, as demonstrated by a melting simulation of SiO_2 where the model correctly reproduces the expected T_{el} dependence of the melting curve (Extended Data Fig. 3). These results confirm that DEM-FF achieves high accuracy and robust generalization across chemically, structurally, and thermodynamically diverse conditions relevant to Earth's interior.

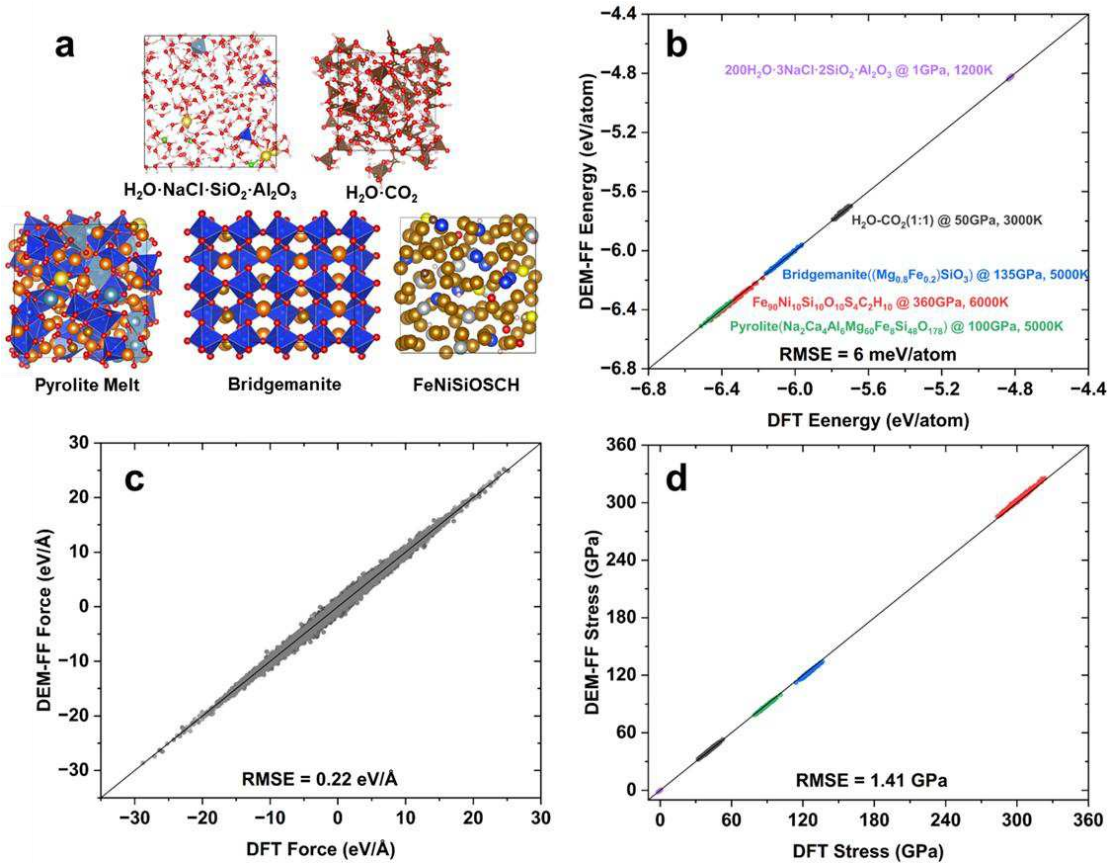


Fig. 2 | Validation of DEM-FF accuracy and transferability across diverse Earth systems.

a. Representative atomic configurations of five validation systems from crust to core conditions: (1) aqueous fluid (1 GPa, 1200 K); (2) deep H_2O-CO_2 fluid (50 GPa, 3000 K); (3) pyrolite melt (100 GPa, 5000 K); (4) Fe-bearing bridgmanite (135 GPa, 5000 K); and (5) liquid Fe-alloy (360 GPa, 6000 K). **b-d**. Parity plots that compare DEM-FF predictions with reference DFT calculations for potential energy (**b**), atomic forces (**c**), and stress (**d**). The validation dataset consists of 100 snapshots extracted from independent 100-ps molecular dynamics trajectories for each system. Low RMSE values (6 meV/atom for energy, 0.22 eV/Å for forces, and 1.41 GPa for stress) confirm accuracy across chemically complex systems from crust to core.

Case study 1: Water solubility in silicate melts from free-energy calculations

Water solubility in silicate melts critically influences magma buoyancy, eruptive dynamics, volatile transport, and mineralization[37–39]. Even small amounts of dissolved H_2O can reduce melt viscosity by orders of magnitude[40]. Experimental solubility data

for water in magma are well established below 1 GPa[38,41–53], which makes the basalt-water system an ideal benchmark for free-energy-based solubility calculations in chemically complex melts.

At equilibrium, water solubility in the silicate melt is determined by equal chemical potential of H_2O in the melt and in the coexisting aqueous phase:

$$\mu_{silicate\ melts}^{H_2O} = \mu_{aqueous\ fluid}^{H_2O} \quad (1)$$

We computed the Gibbs free energy of a basaltic melt with composition $Na_9K_2Ca_{27}Al_{36}Mg_{24}Fe_{15}Si_{96}O_{318}$ at 1600 K for water contents from 0 to 80 H_2O molecules (Methods). The chemical potential of H_2O in the melt was obtained as the derivative of Gibbs free energy with respect to water content at fixed pressure and temperature:

$$\mu_{basalt}^{H_2O} = \left(\frac{\partial G(\text{basalt}+n\cdot H_2O)}{\partial n}\right)_{P,T} \quad (2)$$

Separate simulations of pure water (200 H_2O molecules) provided the reference chemical potential $\mu_{water}^{H_2O}$. This reference assumes negligible dissolution of silicate components into the aqueous phase, an appropriate approximation under the investigated conditions and consistent with experimental observations[54].

The calculated water solubilities are 3.3 wt% at 0.1 GPa, 6.4 wt% at 0.3 GPa, and 8.3 wt% at 0.5 GPa, in good agreement with the experimental values (Fig. 3). This result confirms that DEM-FF can perform reliable absolute free-energy calculations for realistic multi-component melts and demonstrates the feasibility of free-energy-based solubility and partitioning calculations for a broad range of planetary materials.

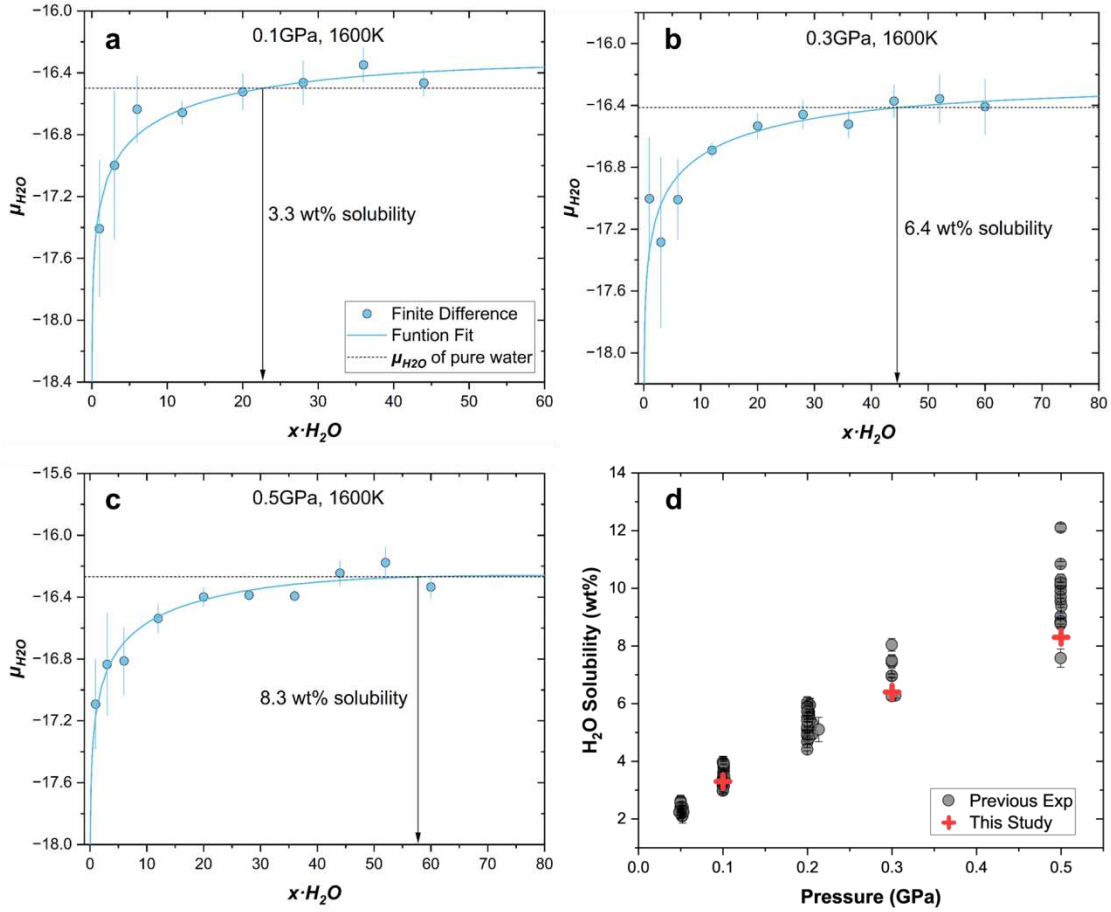


Fig. 3 | Water solubility in basaltic melt derived from free-energy calculations. a-c, Chemical potential of H_2O in basaltic melt as a function of water content at 1600 K for 0.1 GPa (**a**), 0.3 GPa (**b**), and 0.5 GPa (**c**). Blue symbols denote values obtained from finite-difference analysis; solid curves show fitted functions (Methods). The dashed line indicates the chemical potential of pure water at the same conditions. Their intersection defines the solubility limit. **d**, Comparison between calculated solubilities from this study (red crosses) and experimental measurements from the literature[41–53] (gray circles).

Case study 2: Hydrogen Partitioning between Silicate Melt and Liquid Iron

Earth's core is 6-8% less dense than pure iron at the core *P-T* conditions, which implies the presence of one or more light elements[55]. Hydrogen has long been considered a candidate because of its high cosmic abundance and strong solubility in liquid iron at high pressure[24,56–62]. The extent to which hydrogen was incorporated into the core during core formation is governed by its partition coefficient between liquid iron and

256 silicate melt, D_H, a quantity that also bears directly on Earth's volatile budget and the
257 origin of surface water[63,64].
258 Experiments show that D_H is strongly sensitive to oxygen fugacity (fO_2), with more
259 reducing conditions favoring hydrogen incorporation into liquid iron[58,60,61]. In a
260 realistic magma-ocean, fO_2 is coupled to the multicomponent chemistry of both metallic
261 and silicate melts. When this chemistry is neglected, the redox conditions accessed in
262 simulations become biased, and important controls on elemental distribution during
263 metal-silicate differentiation can be obscured[57,65–67]. This bias is particularly apparent
264 in theoretical studies that adopt simplified compositions (e.g., Fe-H binaries for the
265 metal and $MgSiO_3$-H for the silicate), where the redox state is implicitly fixed.
266 Previous theoretical studies have reported widely scattered D_H values, from ~ 10^1
267 to >10^5 at high pressures[24,59]. Much of this variability stems from simplified model
268 systems that lack elements such as O and Si in the metal and Fe in the silicate. These
269 systems tend to sample highly reducing conditions and may overestimate hydrogen
270 partitioning into the metal. Natural metal-silicate systems, by contrast, contain multiple
271 light elements (e.g. O, Si, S, C) that dissolve into iron and interact with H. Hydrogen
272 partitioning in such systems reflects coupled multicomponent chemistry and redox
273 equilibrium. To capture this effect, both phases must be treated with realistic
274 compositions under self-consistent redox conditions, a task that has remained
275 computationally prohibitive for first-principles molecular dynamics (FPMD).
276 We address this challenge by performing direct two-phase coexistence simulations that
277 place both pyrolitic silicate melts and liquid iron within a single simulation cell (Fig. 4a).
278 The efficiency and stability of DEM-FF allow us to simulate multicomponent chemical
279 interactions over a wide pressure range and to evaluate hydrogen partitioning
280 self-consistently under redox conditions set by the bulk system composition.
281 The simulated systems consist of hydrous pyrolite melt ($Na_4Ca_8Al_{12}Mg_{120}Fe_{16}Si_{96}O_{356}$
282 + $16H_2O$) equilibrated with liquid iron containing variable oxygen contents (Fe_{800},
283 $Fe_{800}O_{80}$, $Fe_{800}O_{160}$, $Fe_{800}O_{240}$). Hydrogen partitioning is quantified by the partition
284 coefficient $D_H = C_H^{\text{metal}}/C_H^{\text{silicate}}$, where C_H denotes hydrogen concentration in wt%.
285 Simulations performed from 1 to 135 GPa and 2000 to 5000 K reveal systematic

dependencies of D_H on both pressure and fO_2 (Fig. 5b, c). At 1 GPa, hydrogen is strongly lithophile ($D_H \ll 1$); near 30 GPa, D_H approaches 1, consistent with the experimentally observed transition from lithophile to siderophile behavior around 15-22 GPa[60]. At deep magma-ocean pressures (>100 GPa), hydrogen becomes moderately siderophile, with $D_H \approx$ 2-5 depending on fO_2. At any given pressure, more reducing conditions systematically enhance hydrogen's affinity for the metallic phase.

The combined pressure and fO_2 dependence is well described:

$$logD_H^{m/s} = -0.4536 - 0.226 \cdot \Delta\mathrm{IW} + 0.0022 \cdot P - \frac{53198.8}{1+exp(\frac{P+192.5}{18.34})} \quad (3)$$

where P is pressure in GPa and $\Delta\mathrm{IW} = 2\log(x_{\mathrm{FeO}}^{\mathrm{silicate}}/x_{\mathrm{Fe}}^{\mathrm{metal}})$ represents fO_2 relative to the iron-wüstite buffer. The temperature effect is implicitly included in the pressure term because the temperature increases with the pressure along relevant geotherms. The fitted coefficient for the ΔIW term (-0.226) closely matches the thermodynamic expectation of -0.25 derived from the exchange reaction[58]:

$$\mathrm{HO}_{0.5}^{\mathrm{silicate}} + \frac{1}{2}\mathrm{Fe}^{\mathrm{metal}} \leftrightarrow \mathrm{H}^{\mathrm{metal}} + \frac{1}{2}\mathrm{FeO}^{\mathrm{silicate}} \quad (4)$$

This agreement indicates that the observed trends reflect underlying chemical constraints rather than purely empirical correlations.

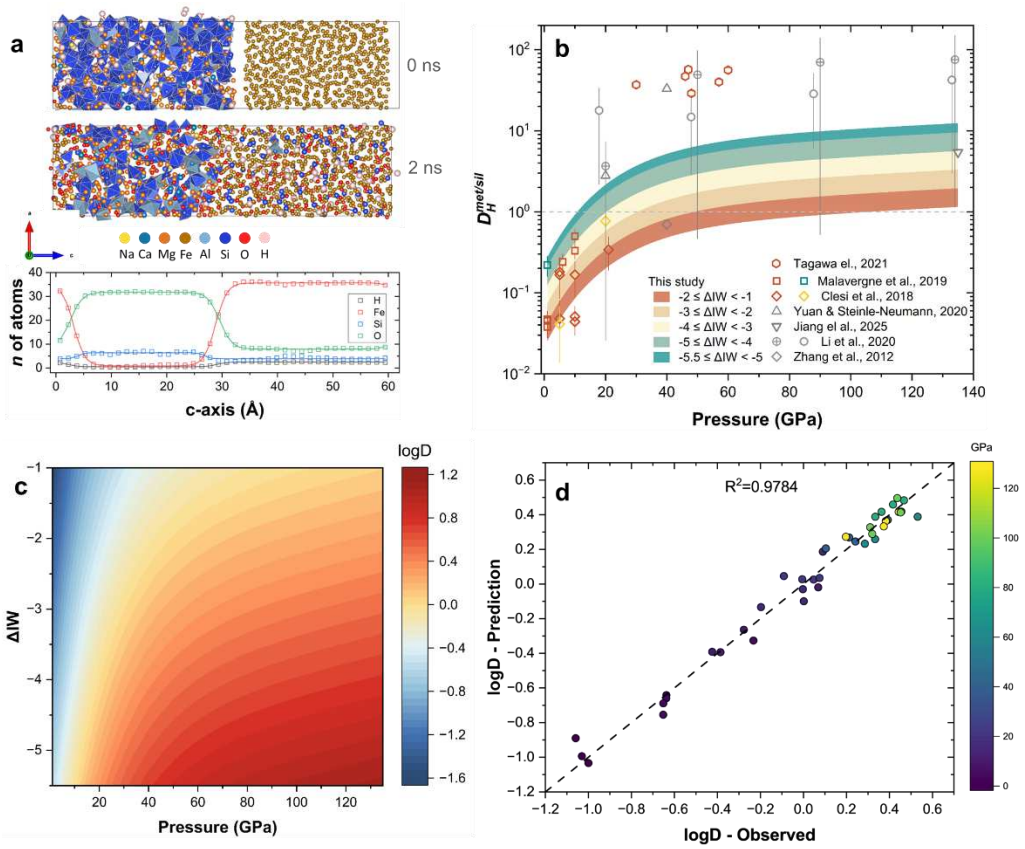


Fig. 4 | Hydrogen partitioning between liquid iron and silicate melt. a, Simulation setup and elemental distributions before and after equilibration, which show the formation of a stable metal-silicate coexisting system. Atomic number density profiles along the cell axis illustrate the distribution of H, Fe, Si, and O across the two-phase interface upon equilibration. **b,** Hydrogen partition coefficient D_H as a function of pressure and fO_2 (Eq. 3). Colored bands represent predictions from this study for different ΔIW ranges; open symbols denote previous experimental and theoretical estimates[24,25,57–62,68]. **c,** Contour map of $\log D_H$ as a function of pressure and ΔIW**. d,** Parity plot compares observed $\log D_H$ values (supplementary data) with predictions from Eq. 3.

Under redox conditions relevant to deep magma ocean (ΔIW ~ -2), our simulations yield $D_H \approx 2$ at 135 GPa. This value is notably lower than predictions from binary Fe-H models but consistent with recent multicomponent simulations that include O and Si in liquid iron[62]. These results demonstrate that dissolved O and Si in metallic liquids suppress hydrogen partitioning and that binary systems systematically overestimate

hydrogen incorporation into the core.

These revised partitioning values provide direct consequences for Earth's hydrogen budget. For core-mantle equilibration at 40-60 GPa[69,70] under $\Delta IW \sim -2$, we obtain a core hydrogen content of approximately 560-840 ppm, corresponding to $1.1\text{-}1.6 \times 10^{21}$ kg of hydrogen, or roughly 7-10 ocean masses of water. Even under the most favourable scenario (complete mantle melting, equilibration above 100 GPa), D_H remains ~2 and core hydrogen does not exceed ~0.14 wt%. Hydrogen therefore contributes to, but cannot account for, the core's 6-8% density deficit; the dominant light-element inventory must comprise other species, most probably some combination of O, Si, S, and C, consistent with cosmochemical constraints and recent experimental partitioning studies.

Discussions

Existing uMLFFs have been trained primarily on crystalline databases assembled under near-ambient conditions. Their coverage of chemical and thermodynamic space therefore reflects this origin. DEM-FF targets a fundamentally different regime: the interior of Earth and other terrestrial planets, where disordered multi-component liquids, reactive metal-silicate interfaces, and pressures up to 360 GPa must all be treated within a single model. To reach this regime, three features distinguish DEM-FF from current uMLFFs: (1) active-learning-driven sampling of a high-dimensional P-T-X-λ space with on-the-fly chemical perturbations, (2) explicit inclusion of thermodynamic-integration intermediate states ($0 < \lambda < 1$) in the training data, and (3) diversity-aware selection that keeps the training set compact (~30,000 configurations) despite the breadth of conditions covered.

The two applications presented above tested DEM-FF against distinct challenges. The first demands accurate absolute free energies for a multi-component melt across a continuous thermodynamic integration state. The second demands stable, long-duration two-phase coexistence simulations with realistic chemistry. The fact that a single model handles both cases without system-specific training validates the methodological

framework underlying DEM-FF. By systematically sampling the *P-T-X-λ* space through active learning, a universal MLFF can be constructed that is both broadly transferable and sufficiently accurate for quantitative geochemical predictions under deep-Earth conditions.

The significance of λ-aware training for geochemical thermodynamics

The quantitative agreement between calculated and experimentally measured H_2O solubility in basaltic melts has broad implications. The success of DEM-FF in this case demonstrates that incorporating λ states in the training data provides the model with reliable free-energy calculation capability. Such capability is fundamental for investigating phase equilibria, element partitioning, volatile solubility, and mineral stability across geochemistry. This capability considerably extends the range of problems accessible to MLFF-based simulations. A natural extension is the prediction of volatile solubility (e.g., C, H, S, N, and noble gases) in silicate melts and volatile partitioning at extreme pressures where experimental data are sparse.

Realistic compositions in element partitioning predictions

Previous theoretical estimates of D_H between metallic and silicate liquids span orders of magnitude from $\sim 10^1$ to $>10^5$ at high pressures. Our multi-component simulations identify the origin of this scatter. In binary Fe-H systems, the absence of oxygen and other light elements in the metallic phase implicitly imposes highly reducing conditions and artificially increases hydrogen's siderophile tendency. When O and Si are present in the metallic liquid, as expected under magma-ocean conditions, they compete with hydrogen for bonding environments and shift the effective redox state of the system. This competition, which our multi-component simulations capture self-consistently, yields $D_H \approx$ 2-5 at pressures above 100 GPa and $\Delta IW \sim$ -2, which are orders of magnitude below the predictions of compositionally simplified models. The fitted ΔIW coefficient (-0.226) closely matches the theoretical expectation of -0.25 from the exchange reaction (Eq. 4), which confirms that our simulation-observed pressure-fO_2 dependence reflects intrinsic thermodynamic equilibrium.

The hydrogen case also illustrates a broader principle. Any element whose metal-silicate partitioning is sensitive to redox conditions or to competition with co-dissolved

solutes may be systematically mischaracterized by simplified model systems. C, N, S, and moderately siderophile elements such as W are likely subject to similar effects. The same principle applies to the silicate phase, as natural magmas contain Ca, Al, Na, K, Fe, and dissolved volatiles, each of which modifies melt structure, speciation, and thermodynamic activity coefficients. The pyrolitic composition employed in our simulations ($Na_4Ca_8Al_{12}Mg_{120}Fe_{16}Si_{96}O_{356}$) captures this chemical complexity, which has been computationally prohibitive to treat with FPMD, where system sizes typically do not exceed a few hundred atoms and simulation durations reach only tens of picoseconds. DEM-FF makes such compositionally realistic simulations tractable at the system sizes and timescales required for equilibrated partitioning calculations, which allows direct comparison with natural and experimental systems.

Limitations and outlook

Although DEM-FF demonstrates broad applicability across deep-Earth conditions, several limitations deserve discussion. DEM-FF inherits the systematic biases of the PBEsol functional used to generate its training data, including known limitations in the treatment of van der Waals interactions and strongly correlated electronic states[71]. Nevertheless, at the pressures and temperatures relevant to deep-Earth, dispersion effect contributions to total energies become comparatively minor, and semi-empirical corrections such as DFT-D3[72] can be readily applied with DEM-FF. The treatment of strongly correlated electrons presents a more fundamental challenge. Our training data were generated with spin-polarized DFT calculations, which capture partial effects of magnetic ordering and spin-state energetics. However, incorporating spin degrees of freedom explicitly into the MLFF architecture and enabling the model to predict spin-dependent potential energy surfaces remain active frontiers in MLFF development[73,74]. Future improvements could also benefit from incorporating training data from meta-GGA[75] or hybrid functionals[76], though the computational cost of generating such dataset at the scale required for a universal model remains considerable. The current 25-element included in DEM-FF, while covering the major rock-forming and volatile elements, excludes several species of geochemical importance, such as platinum-group elements[77], rare earth elements[78], and radioactive species (U, Th) central to

geochronology and heat-production estimates[79]. Extending elemental coverage is procedurally straightforward but requires dedicated DFT data generation and active-learning cycles for each new element group.

Finally, we note that DEM-FF can serve as a foundation model for system-specific refinement[80]. Researchers requiring higher accuracy for particular compositions or conditions can fine-tune the model with a small set of higher-fidelity training data, which is substantially more efficient than constructing a dedicated force field from scratch. As additional training data for new compositions and thermodynamic conditions become available, the model's coverage and reliability will continue to improve. Extensions to other terrestrial planets, whose interior compositions, redox profiles, and volatile inventories differ from Earth's, represent a particularly promising direction for future work.

Conclusion

We have presented DEM-FF, a universal machine-learning force field for DFT-level simulations of deep-Earth materials across planetary interior conditions. Its broad applicability has the potential to transform the conventional workflow in computational mineral physics, where developing a new, specialized force field for each scientific problem is typically time-consuming. By removing this requirement, DEM-FF can be applied directly to a range of key planetary processes, including volatile solubility and cycling, core-mantle differentiation, metal-silicate element partitioning, and high-pressure phase equilibria.

Methods

Machine Learning Force Field Architecture

DEM-FF employs the MACE-LES architecture[27,28], which integrates equivariant message-passing with higher-order tensor-product features to capture complex atomic environments, and a Latent Ewald Summation (LES) layer to handle long-range electrostatic interactions. To accurately model high-temperature electronic effects typical of deep-Earth conditions, we incorporated the electronic temperature (T_{el}) as an additional parameter integrated into the message-passing blocks. This allows the model to learn the dependence of the potential energy surface on electronic entropy, which has been proved essential for accurately determining phase stabilities under deep-Earth conditions[33–36].

The model comprises two message-passing layers with a cutoff of 4.5 Å, an embedding dimension of 256, and a maximum angular momentum L_{max} = 3. With two message-passing layers, local atomic information can propagate effectively over a distance of 9 Å. We trained the model by minimizing a weighted mean-squared-error (*MSE*) loss function that combines energies (E), forces (F), and stresses (S),

$$\mathcal{L} = w_E \,\mathrm{MSE}(E) + w_F \,\mathrm{MSE}(F) + w_S \,\mathrm{MSE}(S) \qquad (5)$$

Training was performed in two stages. In the first stage, we prioritized force accuracy ($w_E = 1.0,\ w_F = 100.0,\ w_S = 1.0$). In the second stage, we increased the weights of energy and stress ($w_E = 1000.0, w_S = 10.0$) while maintaining $w_F = 100.0$ to refine energy and stress predictions.

Density Functional Theory Calculations

We performed first-principles molecular dynamics (FPMD) simulations and generated training data using density functional theory (DFT) as implemented in VASP[81,82]. We employed the projector augmented wave (PAW) method[83] and the PBEsol exchange-correlation functional[84]. PAW potentials were used for all 25 elements in this study (Na_sv, K_sv, Ca_sv, Al_sv, Mg_pv, Fe_sv, Si, O, H, C, N, S, He, Ne, Ar, Kr, Xe, B, P, F, Cl, Ti_sv, Mn_sv, Ni_sv and W_sv). A plane-wave cutoff of 600 eV and Γ-point

sampling were employed. We also included spin polarization for all transitional metal elements, and electronic occupancies were determined using a Fermi-Dirac distribution to properly account for electronic temperature effects. The electronic self-consistency was converged to 10^{-6} eV.

MD Simulations and H Partitioning

All molecular dynamics (MD) simulations were performed using the Atomic Simulation Environment (ASE)[85]. Two-phase metal-silicate coexistence simulations ran in the NVT ensemble using a Nosé-Hoover thermostat with a timestep of 0.5 fs. Production runs consisted of 0.5 ns equilibration followed by 2 ns of sampling. Target pressures were achieved by adjusting the simulation cell volume.

We calculated elemental concentration profiles perpendicular to the metal-silicate interface by time-averaging atomic number densities using the Gibbs dividing surface method[86]. Oxygen fugacity (fO_2) relative to the iron-wüstite (IW) buffer was derived from the mol concentration of FeO in the silicate melt and Fe in the metal phase.

To estimate the core hydrogen content ($C_{\mathrm{H}}^{\mathrm{core}}$) derived from magma ocean equilibration, we utilized a mass balance method based on the calculated partition coefficient $D_{\mathrm{H}} = C_{\mathrm{H}}^{\mathrm{metal}}/C_{\mathrm{H}}^{\mathrm{silicate}}$:

$$C_{\mathrm{H}}^{\mathrm{core}} = \frac{C_{\mathrm{H}}^{\mathrm{total}} \cdot M_{\mathrm{Earth}}}{M_{\mathrm{core}} + M_{\mathrm{mantle}}/D_{\mathrm{H}}} \qquad (6)$$

where $C_{\mathrm{H}}^{\mathrm{total}}$ is the bulk earth water inventory assumption (mapped to H mass), and mass fractions are standard Earth reference values.

First-Principles Training Data Generation

1. Initial Dataset Construction

We constructed an initial training dataset that targets five material classes representing the major phases and chemical environments of Earth.

(1) Fluids and volatiles: We selected simple molecular species and their mixtures to represent volatile components relevant to Earth's interior, including H_2, H_2O, CO,

CO_2, CH_4, NH_3, N_2, NO, NO_2, H_2S, S_2, SO, SO_2, SO_3, noble gases, and their mixtures.

(2) Mantle minerals: The dataset includes representative mineral phases from the upper mantle (olivine, pyroxenes, garnets), transition zone (wadsleyite, ringwoodite), and lower mantle (bridgmanite, davemaoite, periclase, post-perovskite).

(3) Silicate melts: We constructed 40 silicate melt compositions within the Na_2O-K_2O-CaO-MgO-FeO-Al_2O_3-SiO_2-TiO_2-P_2O_5-volatile system. Volatile (see above) contents vary from 0 to 30 wt%, and SiO_2 contents range from 30 to 80 wt%, covering a broad composition from felsic to ultramafic, from volatile-poor to volatile-rich magmatic system.

(4) Iron phases: Liquid iron and solid iron phases with body-centered cubic (bcc), face-centered cubic (fcc), and hexagonal close-packed (hcp) structures were included to represent Earth's core materials.

(5) Artificial multicomponent random systems: To systematically explore chemical interactions beyond equilibrium environments, we incorporated artificial multicomponent systems constructed within the full 25-element space. We constructed 25 unitary, 300 binary, 400 ternary (randomly selected from 2,300 combinations), and 400 quaternary systems (from 12,650 combinations) with atoms randomly placed on cubic lattice sites. These configurations allow the model to learn diverse atomic interactions and high-order multicomponent effects[87].

All initial configurations were subjected to FPMD simulations for 2,000 timesteps across pressures from 0 to 360 GPa and temperatures from 300 to 10,000 K.

2. Iterative Training Data Refinement

Starting from the initial dataset, we employed an active learning framework to iteratively refine the training dataset. Each iteration involved 4 steps:

(1) Ensemble training: We trained four independent MACE models with different random initializations on the current dataset.

(2) Exploration of *P-T-X-λ* space: We used the trained ensemble of models to perform extensive MD simulations across a dense grid of pressure (0-360 GPa, 10 GPa intervals), temperature (300-10,000 K, 500 K intervals), composition, and coupling

parameter (λ = 0.0, 0.1, 0.2, ..., 1.0). At the beginning of each exploration, we regenerated the compositions of the five systems mentioned above and used them as input configurations for MD simulations. To further enhance the sampling efficiency of the compositional dimension, we applied on-the-fly chemical perturbations during the simulations. These perturbations include elemental substitutions, insertions, and removals that drive the system into new chemical environments.

Specifically, aqueous systems were doped with dissolved species such as NaCl, SiO_2, Al_2O_3, HF, $CaCO_3$ and H_2SO_4. Mantle minerals underwent charge-balanced substitutions, including but not limited to $Mg^{2+} \leftrightarrow Fe^{2+} \leftrightarrow Ca^{2+} \leftrightarrow 2H^{+}$, $Si^{4+} \leftrightarrow Ti^{4+}$, and $Mg^{2+} + Si^{4+} \leftrightarrow 2Al^{3+}$, as well as Schottky defect formation such as paired Mg and O vacancies. Silicate melts experienced similar charge-balanced substitutions and incorporated volatile species such as H_2O and CO_2 during simulations. Iron systems allowed substitution of Fe by any of the other 24 elements to generate diverse alloy compositions. Noble gases were incorporated into all systems through interstitial insertion or substitutional mechanisms, including Xe substitution for Si or Mg[88,89]. These procedures make sure that local atomic chemical environments and compositional space can be sampled as diverse as possible within each single exploration simulation.

(3) Uncertainty quantification: We quantified force uncertainty using the standard deviation of predicted atomic forces across the four models. Configurations where the maximum force standard deviation exceeded a threshold of 0.35 eV/Å were identified as high-uncertainty candidates and were selected for further evaluation.

(4) Diversity-aware selection and Labeling: To minimize the size of the training dataset while maintaining its broad chemical environment coverage, we applied principal component analysis (PCA) to the 256-dimensional MACE atomic descriptors, reducing them to approximately 10 principal components that capture over 95% of the total variance. Farthest-point sampling (FPS) was then applied within this reduced space to select a diverse subset (e.g., 10%) of the candidate configurations. These selected structures were then evaluated with static DFT calculations to obtain energies, forces, and stresses. The newly labeled data were incorporated into the training dataset

for the subsequent iteration.

We repeated this iteration 12 times until the force uncertainties converged. The final DEM-FF model was trained on over 30,000 atomic configurations.

Free Energy Calculations

Absolute Helmholtz free energies were computed via nonequilibrium thermodynamic integration (NETI)[90,91], in which the system is continuously switched between a reference Hamiltonian with known analytical free energy and the target DEM-FF Hamiltonian along a coupling parameter $\lambda \in [0, 1]$.

For liquid phases, the Uhlenbeck-Ford model (UFM)[92] was adopted as the reference potential. The UFM is a soft, purely repulsive pair potential defined as:

$$\mathrm{UFM}(r) = -pk_bTln[1 - exp(-r^2/\sigma^2)] \qquad (7)$$

where p is a dimensionless exponent that controls the steepness of the repulsion, σ is the length-scale parameter, r is inter-atomic distance, and T is the temperature. For all calculations in this study, we used p = 50 and σ = 1.2 Å, with a pair-interaction cutoff at $r_{cut} = 5\sigma$ = 6.0 Å. The analytical excess free energy of the UFM fluid is available from the spline-interpolated equation of state[90,92]. The total liquid free energy simulated by DEM-FF is then obtained as

$$F_{\mathrm{DEM\text{-}FF}} = F_{\mathrm{ideal}} + F_{\mathrm{ideal}\rightarrow\mathrm{UFM}} + \Delta F_{\mathrm{UFM}\rightarrow\mathrm{DEM\text{-}FF}} \qquad (8)$$

where F_{ideal} is the ideal Helmholtz free energy, $F_{\mathrm{ideal}\rightarrow\mathrm{UFM}}$ is the excess free energy of the UFM fluid, $\Delta F_{\mathrm{UFM}\rightarrow\mathrm{DEM\text{-}FF}}$ is the free energy difference between the UFM and DEM-FF, which is computed via NETI.

The Gibbs free energy was then obtained from the standard thermodynamic relation

$$G(P,T) = F_{\mathrm{DEM\text{-}FF}}(P,T) + PV \qquad (9)$$

Chemical potential of water in silicate melt

The chemical potential of water dissolved in basaltic melt is derived from the concentration dependence of the Gibbs free energy. For a basaltic system containing x water molecules at fixed pressure and temperature, the Gibbs free energy is written as

$$G(x) = F(x) + PV(x) \qquad (10)$$

The Helmholtz free energy can be decomposed into a ideal contribution and a residual term,

$$F(x) = F_{\mathrm{id}}(x) + F_{\mathrm{res}}(x) \qquad (11)$$

where F_{id} is the ideal Helmholtz free energy and F_{res} accounts for all non-ideal interactions. The corresponding Gibbs free energy can be written as

$$G(x) = F_{\mathrm{id}}(x) + G_{\mathrm{res}}(x) \qquad (12)$$

Here, $G_{\mathrm{res}}(x)$ is evaluated using the NETI method described above, while $F_{\mathrm{id}}(x)$ is calculated analytically as

$$F_{id}(x) = k_B T \sum_{i=1}^{n} (ln \frac{N_i \Lambda_i^3}{V(x)} - 1) \qquad (13)$$

where the sum runs over all atomic species, and N_i denotes the number of atoms of species i, and $\Lambda_i = h/2\pi m_i k_B T$ is the thermal de Broglie wavelength.

The chemical potential of water is defined as

$$\mu_{H_2O}^{\mathrm{basalt}} = \left(\frac{\partial G(x)}{\partial x}\right)_{P,T} \qquad (14)$$

Over the investigated concentration range, the equilibrium volume and residual Gibbs free energy vary smoothly with water content and were fitted using second-order polynomials,

$$V(x) = V_0 + ax + bx^2 \quad and \; G_{\mathrm{res}}(x) = c + dx + ex^2 \qquad (15)$$

The final expression for the chemical potential is therefore

$$\mu_{H_2O}^{\mathrm{basalt}} = \frac{\partial F_{\mathrm{id}}(x)}{\partial x} + d + 2ex \qquad (16)$$

where $\frac{\partial F_{id}(x)}{\partial x} = k_B T[ln \frac{N_O(x) \Lambda_O^3}{V(x)} + 2ln \frac{N_H(x) \Lambda_H^3}{V(x)} - \frac{N_{total}(x)}{V(x)} V'(x)]$.

Data availability

The DFT training data used in this work were generated using the Vienna *Ab-initio* Simulation Package (VASP; https://www.vasp.at). Machine-learning force fields were trained with the MACE-LES framework (https://github.com/ACEsuit/mace), and all simulations and active learning workflows were performed using the Atomic

Simulation Environment (ASE; https://ase-lib.org).

The trained DEM-FF models and associated input files will be made publicly available upon publication.

Acknowledgments

This work was supported by National Natural Science Foundation of China (grant number 42421002, T2495234, 41602032) and National Key R&D Program of China (grant number 2022YFF0800403). The calculation was performed using the computing facilities at the High-Performance Computing Center (HPCC) of Nanjing University and Beijing PARATERA Technology Co., LTD.

Author contributions

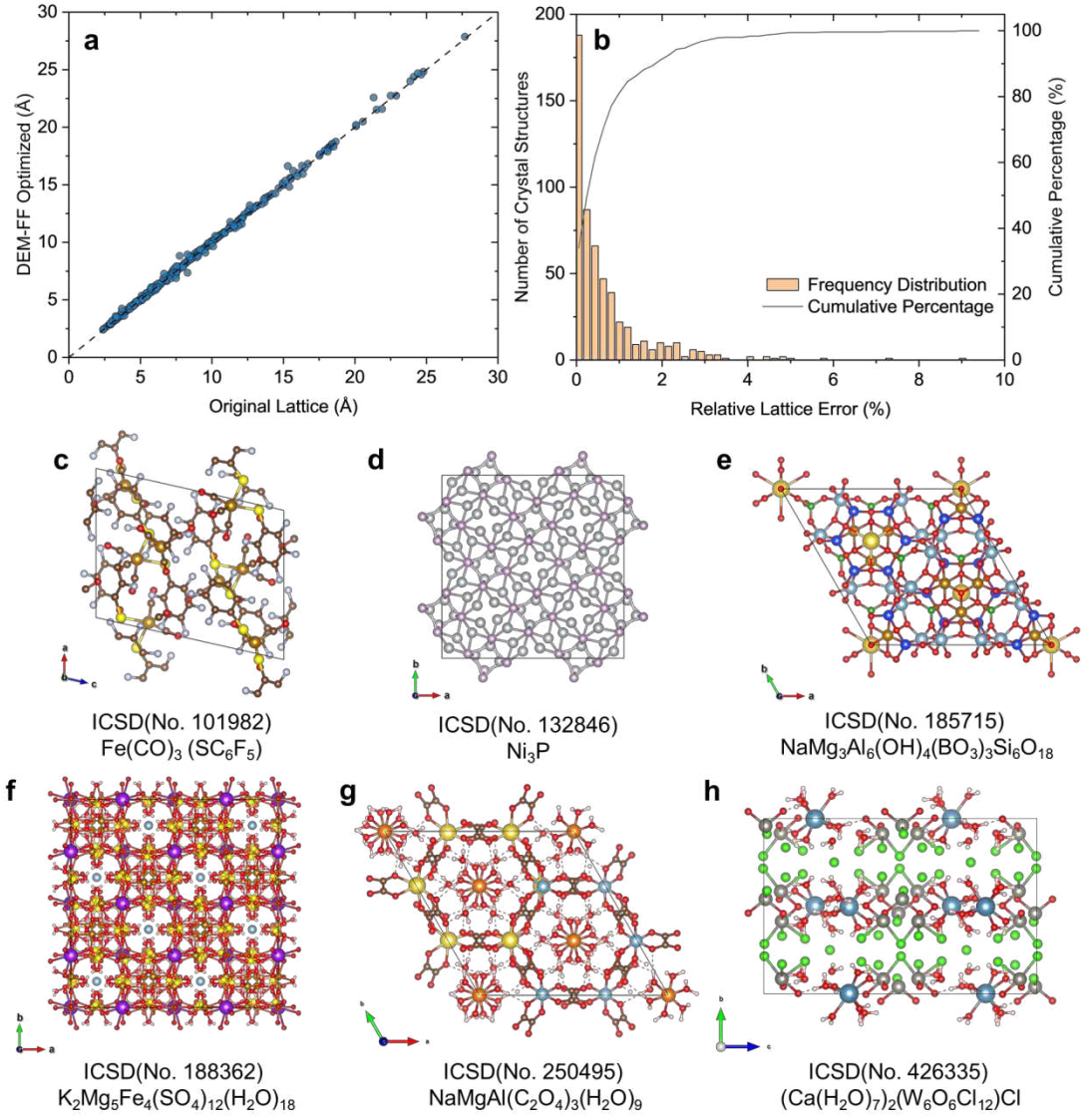
K.W. and X. L. conceived the project. K.W. and Y.C.Z performed the force-field development and MD simulations. All authors discussed the results and wrote the manuscript.

Competing interests

The authors declare no competing interests.

Additional information

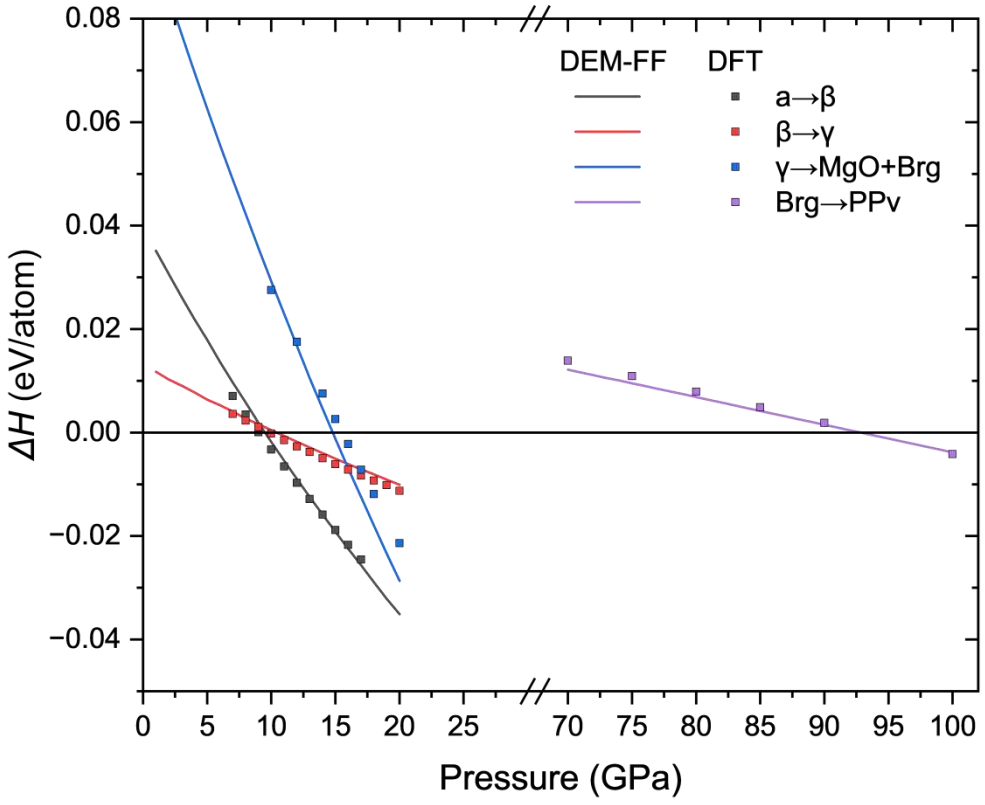
Correspondence and requests for materials should be addressed to Xiancai Lu (xcljun@nju.edu.cn).



Extended Data Fig. 1. | Out-of-distribution structural validation of DEM-FF on crystalline materials.

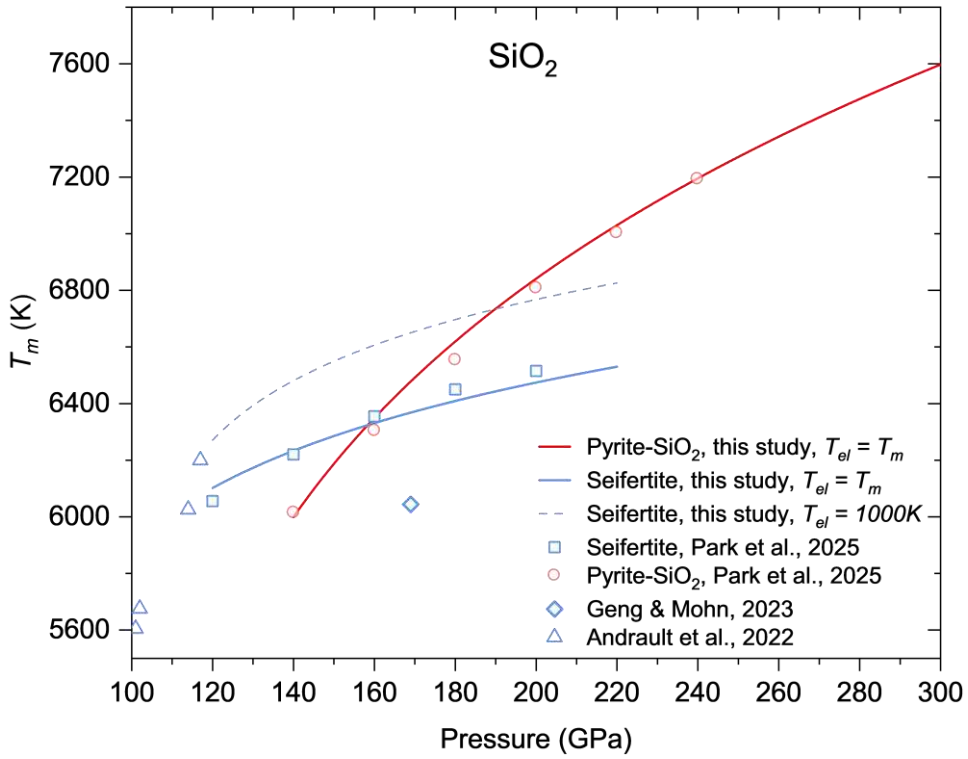
a, Comparison between DEM-FF's prediction and experimental lattice parameters for 553 inorganic crystal structures from the ICSD. **b**, Distribution of relative lattice parameter errors. Over 80% of the structures are reproduced within 1% error and ~ 99% within 5%. The three structures with errors exceeding 5% are triangular close-packed layered carbon allotrope (ICSD 28857), solid HCl (ICSD 28844) and δ-P_4 white phosphorus (ICSD 148325). In all three cases, the dominant cohesive interactions between structural units (layers or molecules) are weak van der Waals interactions that are notoriously difficult for semi-local DFT functionals and, by extension, for MLFFs trained on such data; **c-h**, Representative crystal structures with relative

lattice-parameter errors below 1%, which illustrate DEM-FF's ability to generalize to chemically and structurally complex systems absent from training. **c**, organometallic complex: $Fe(CO)_3(SC_6F_5)$; **d**, meteoritic phosphide schreibersite: Ni_3P; **e**, fluor-schorl tourmaline: $NaMg_3Al_6(OH)_4(BO_3)_3Si_6O_{18}$; **f**, hydrated sulfate voltaite: $K_2Mg_5Fe_4(SO_4)_{12}(H_2O)_{18}$; **g**, heterometallic oxalate hydrate: $NaMgAl(C_2O_4)_3(H_2O)_9$; and **h**, supramolecular tungsten cluster compound featuring an octahedral W_6 core: $(Ca(H_2O)_7)_2(W_6O_6Cl_{12})Cl$.



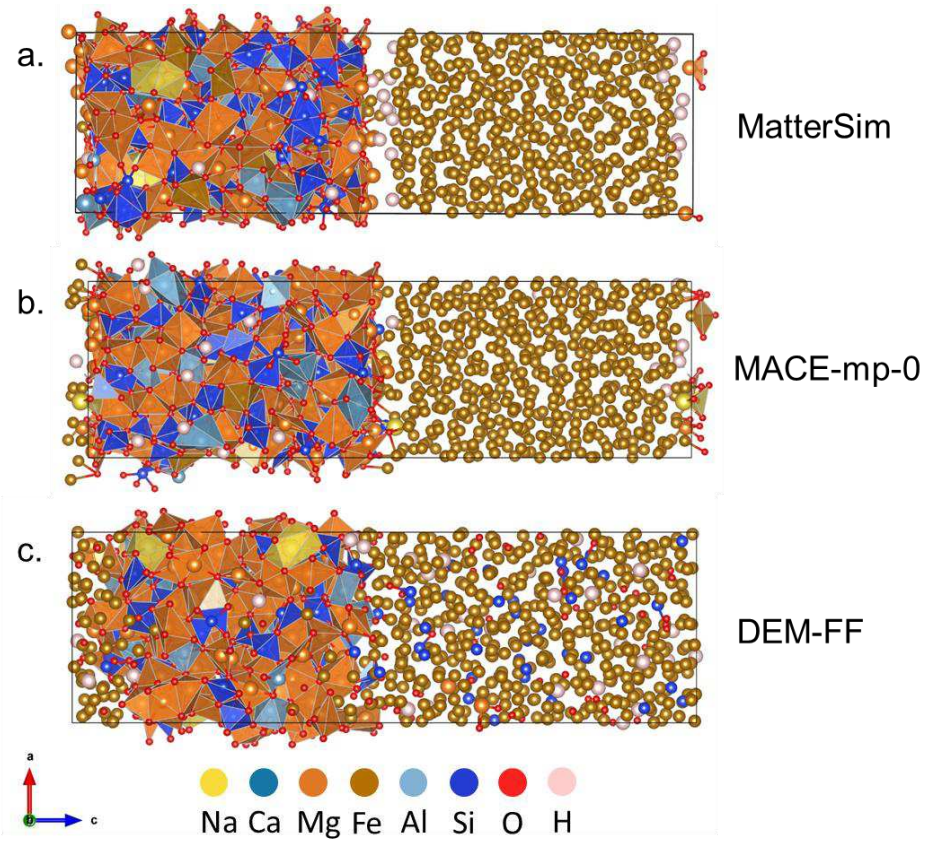
Extended Data Fig. 2 | Phase transition of major mantle minerals at 0K from enthalpy calculations.

Relative enthalpies of major Mg-Si-O mantle mineral phases as a function of pressure at 0 K, calculated using PBEsol-DFT (symbols) and DEM-FF (lines). The phase transitions from upper mantle to the lowermost mantle, include olivine (α-Mg_2SiO_4) → wadsleyite (β-Mg_2SiO_4) → ringwoodite (γ-Mg_2SiO_4) → MgO + $MgSiO_3$-bridgmanite (Brg), and the transition from bridgmanite to post-perovskite $MgSiO_3$ (PPv). Phase boundaries are determined from enthalpy difference between two phases $\Delta H = 0$. The DEM-FF reproduces relative phase stability across the pressure range of Earth's interior in good agreement with the DFT calculation.



Extended Data Fig. 3 | Melting curves of high-pressure SiO_2 phases.

Melting temperatures (T_m) of seifertite and pyrite-type SiO_2were determined using the two-phase method with the DEM-FF. Electronic-temperature (T_{el}) effect was considered. For pyrite-type SiO_2, simulations were performed with $T_{el} = T_m$ (solid red line). For seifertite, two settings were considered: (i) $T_{el} = T_m$ (solid blue line) and (ii) T_{el} fixed at 1000 K (dashed blue line). The $T_{el} = T_m$ setting yields systematically lower melting temperatures (~150 to 300 K) than T_{el} =1000 K for seifertite, consistent with the expected electronic-entropy stabilization of the liquid at elevated T_{el} reported in previous studies[35]. Melting data for SiO_2 based on MLFF simulation[93], DFT calculation[35] and DAC experiment[94] are shown for comparison. Melting curves were fitted using Simon-Glatzel equation: $T_m(P) = T_0[1 + (P - P_0)/a]^b$, where P is in GPa, *a, b,* T_0, P_0 are fit parameters. For seifertite: T_0 = 6101.9 ± 15.9, P_0 = 120.0, a = 44.9 ± 20.9, b = 17.2 ± 4.7; for pyrite-type SiO_2: T_0 = 5999.2 ± 48.5, P_0 = 140.0, a = 46.4 ± 15.5, b = 6.3 ± 1.1.



680

681 **Extended Data Fig. 4 | Comparison of hydrous silicate melt-liquid iron two-phase**
682 **coexistence simulations using different universal MLFFs at 40 GPa and 3500 K.**
683 Snapshots after 1 ns equilibration of hydrous pyrolite melt coexisting with liquid iron,
684 simulated with **a**, MatterSim[18]; **b**, MACE-MP-0 (medium)[15]; and **c**, DEM-FF. All three
685 simulations start from the same initial configuration. **a**, MatterSim produces an
686 unphysical phase separation in which hydrogen atoms segregate into a distinct layer at
687 the melt-metal interface, contrary to all experimental observations at these conditions.
688 **b**, MACE-MP-0 maintains two-phase coexistence but yields an essentially inert
689 interface that neither silicate components (Si, O) nor hydrogen enter the metallic phase,
690 which also fails to reproduce the well-established solubility of light elements in liquid
691 iron at high pressure. **c**, DEM-FF correctly captures the chemical reactivity of the metal-
692 silicate, with substantial amounts of Si and O dissolving into the liquid iron phase, and
693 hydrogen preferentially partitions into the metal.
694

References

1. Behler, J. & Parrinello, M. Generalized Neural-Network Representation of High-Dimensional Potential-Energy Surfaces. *Phys. Rev. Lett.* **98**, 146401 (2007).
2. Behler, J. Perspective: Machine learning potentials for atomistic simulations. *The Journal of Chemical Physics* **145**, 170901 (2016).
3. Deringer, V. L. *et al.* Gaussian Process Regression for Materials and Molecules. *Chemical Reviews* **121**, 10073–10141 (2021).
4. Unke, O. T. *et al.* Machine Learning Force Fields. *Chem. Rev.* **121**, 10142–10186 (2021).
5. Friederich, P., Häse, F., Proppe, J. & Aspuru-Guzik, A. Machine-learned potentials for next-generation matter simulations. *Nat. Mater.* **20**, 750–761 (2021).
6. Peng, Y. & Deng, J. Thermal Conductivity of $MgSiO_3$ -H_2 O System Determined by Machine Learning Potentials. *Geophysical Research Letters* **51**, e2023GL107245 (2024).
7. Wang, D., Wu, Z. & Deng, X. Thermal conductivity of Fe-bearing bridgmanite and post-perovskite: Implications for the heat flux from the core. *Earth and Planetary Science Letters* **621**, 118368 (2023).
8. Wang, K., Lu, X., Liu, X. & Yin, K. Noble gas (He, Ne, and Ar) solubilities in high-pressure silicate melts calculated based on deep-potential modeling. *Geochimica et Cosmochimica Acta* **350**, 57–68 (2023).
9. Deng, J. & Stixrude, L. Thermal Conductivity of Silicate Liquid Determined by Machine Learning Potentials. *Geophysical Research Letters* **48**, e2021GL093806 (2021).
10. Zhang, Z., Csányi, G. & Alfè, D. Partitioning of sulfur between solid and liquid iron under Earth's core conditions: Constraints from atomistic simulations with machine learning potentials. *Geochimica et Cosmochimica Acta* **291**, 5–18 (2020).
11. Zhang, Z. *et al.* Oxygen Driving Hydrogen Into the Inner Core: Implications for the Earth's Core Composition. *Geophysical Research Letters* **52**, e2024GL110315 (2025).
12. Cheng, B., Hamel, S. & Bethkenhagen, M. Thermodynamics of diamond formation from hydrocarbon mixtures in planets. *Nat Commun* **14**, 1104 (2023).
13. Chen, C. & Ong, S. P. A universal graph deep learning interatomic potential for the periodic table. *Nat Comput Sci* **2**, 718–728 (2022).
14. Deng, B. *et al.* CHGNet as a pretrained universal neural network potential for charge-informed atomistic modelling. *Nat Mach Intell* **5**, 1031–1041 (2023).
15. Batatia, I. *et al.* A foundation model for atomistic materials chemistry. Preprint at https://doi.org/10.48550/arXiv.2401.00096 (2024).
16. Neumann, M. *et al.* Orb: A Fast, Scalable Neural Network Potential. Preprint at https://doi.org/10.48550/arXiv.2410.22570 (2024).
17. Xie, F., Lu, T., Meng, S. & Liu, M. GPTFF: A high-accuracy out-of-the-box universal AI force field for arbitrary inorganic materials. *Science Bulletin* **69**, 3525–3532 (2024).
18. Yang, H. *et al.* MatterSim: A Deep Learning Atomistic Model Across Elements, Temperatures and Pressures. Preprint at https://doi.org/10.48550/arXiv.2405.04967 (2024).
19. Zhang, D. *et al.* DPA-2: a large atomic model as a multi-task learner. *npj Comput Mater* **10**, 293 (2024).
20. Horton, M. K. *et al.* Accelerated data-driven materials science with the Materials Project. *Nat. Mater.* **24**, 1522–1532 (2025).
21. Jinnouchi, R., Karsai, F. & Kresse, G. Making free-energy calculations routine: Combining first

principles with machine learning. *Phys. Rev. B* **101**, 060201 (2020).
22. Yuan, L. & Steinle-Neumann, G. Earth's "Missing" Chlorine May Be in the Core. *JGR Solid Earth* **129**, e2023JB027731 (2024).
23. Wang, K., Lu, X., Liu, X., Zhou, M. & Yin, K. Partitioning of noble gases (He, Ne, Ar, Kr, Xe) during Earth's core segregation: A possible core reservoir for primordial noble gases. *Geochimica et Cosmochimica Acta* **321**, 329–342 (2022).
24. Li, Y., Vočadlo, L., Sun, T. & Brodholt, J. P. The Earth's core as a reservoir of water. *Nat. Geosci.* **13**, 453–458 (2020).
25. Luo, H., Zheng, D. & Deng, J. Earth's core-mantle differentiation shaped by water. *Sci. Adv.* **11**, eadu2952 (2025).
26. Oganov, A. R. & Ono, S. Theoretical and experimental evidence for a post-perovskite phase of MgSiO3 in Earth's D" layer. *Nature* **430**, 445–448 (2004).
27. Batatia, I., Kovács, D. P., Simm, G. N. C., Ortner, C. & Csányi, G. MACE: higher order equivariant message passing neural networks for fast and accurate force fields. in *Proceedings of the 36th International Conference on Neural Information Processing Systems* (Curran Associates Inc., Red Hook, NY, USA, 2022).
28. King, D. S., Kim, D., Zhong, P. & Cheng, B. Machine learning of charges and long-range interactions from energies and forces. *Nat Commun* **16**, 8763 (2025).
29. Zhang, Y. *et al.* DP-GEN: A concurrent learning platform for the generation of reliable deep learning based potential energy models. *Computer Physics Communications* **253**, 107206 (2020).
30. Deng, J., Niu, H., Hu, J., Chen, M. & Stixrude, L. Melting of MgSi O 3 determined by machine learning potentials. *Phys. Rev. B* **107**, 064103 (2023).
31. Deng, J., Niu, H., Hu, J., Chen, M. & Stixrude, L. Melting of MgSi O 3 determined by machine learning potentials. *Phys. Rev. B* **107**, 064103 (2023).
32. Rühl, S. The Inorganic Crystal Structure Database (ICSD): A Tool for Materials Sciences. in *Materials Informatics* (eds Isayev, O., Tropsha, A. & Curtarolo, S.) 41–54 (Wiley, 2019). doi:10.1002/9783527802265.ch2.
33. Belonoshko, A. B., Fu, J. & Smirnov, G. Free energies of iron phases at high pressure and temperature: Molecular dynamics study. *Phys. Rev. B* **104**, 104103 (2021).
34. Ghosh, M., Zhang, S., Hu, L. & Hu, S. X. Cooperative diffusion in body-centered cubic iron in Earth and super-Earths' inner core conditions. *J. Phys.: Condens. Matter* **35**, 154002 (2023).
35. Geng, M. & Mohn, C. E. Influence of electronic entropy on Hellmann-Feynman forces in *ab initio* molecular dynamics with large temperature changes. *Phys. Rev. B* **108**, 134110 (2023).
36. Wu, F. *et al.* Melting temperature of iron under the Earth's inner core condition from deep machine learning. *Geoscience Frontiers* **15**, 101925 (2024).
37. Mysen, B. Water-melt interaction in hydrous magmatic systems at high temperature and pressure. *Prog Earth Planet Sci* **1**, 4 (2014).
38. Papale, P., Moretti, R. & Paonita, A. Thermodynamics of Multi-component Gas–Melt Equilibrium in Magmas: Theory, Models, and Applications. *Reviews in Mineralogy and Geochemistry* **87**, 431–556 (2022).
39. Xie, L. *et al.* Mineralogical constraints on the genesis of W–Nb–Ta mineralization in the Laiziling granite (Xianghualing district, south China). *Ore Geology Reviews* **95**, 695–712 (2018).
40. Sun, Y., Liu, X. & Lu, X. Structures and transport properties of supercritical SiO2-H2O and NaAlSi3O8-H2O fluids. *American Mineralogist* **108**, 1871–1880 (2023).

41. Vetere, F., Holtz, F., Behrens, H., Botcharnikov, R. E. & Fanara, S. The effect of alkalis and polymerization on the solubility of H2O and CO2 in alkali-rich silicate melts. *Contrib Mineral Petrol* **167**, 1014 (2014).
42. Shishkina, T. A. *et al.* Compositional and pressure effects on the solubility of H2O and CO2 in mafic melts. *Chemical Geology* **388**, 112–129 (2014).
43. Iacono-Marziano, G., Morizet, Y., Le Trong, E. & Gaillard, F. New experimental data and semi-empirical parameterization of H2O–CO2 solubility in mafic melts. *Geochimica et Cosmochimica Acta* **97**, 1–23 (2012).
44. Vetere, F., Botcharnikov, R. E., Holtz, F., Behrens, H. & De Rosa, R. Solubility of H2O and CO2 in shoshonitic melts at 1250°C and pressures from 50 to 400MPa: Implications for Campi Flegrei magmatic systems. *Journal of Volcanology and Geothermal Research* **202**, 251–261 (2011).
45. Lesne, P., Scaillet, B., Pichavant, M., Iacono-Marziano, G. & Beny, J.-M. The H2O solubility of alkali basaltic melts: an experimental study. *Contrib Mineral Petrol* **162**, 133–151 (2011).
46. Shishkina, T. A., Botcharnikov, R. E., Holtz, F., Almeev, R. R. & Portnyagin, M. V. Solubility of H2O- and CO2-bearing fluids in tholeiitic basalts at pressures up to 500MPa. *Chemical Geology* **277**, 115–125 (2010).
47. Stelling, J., Botcharnikov, R. E., Beermann, O. & Nowak, M. Solubility of H2O- and chlorine-bearing fluids in basaltic melt of Mount Etna at T= 1050–1250 °C and P= 200 MPa. *Chemical Geology* **256**, 102–110 (2008).
48. Schmidt, B. C. & Behrens, H. Water solubility in phonolite melts: Influence of melt composition and temperature. *Chemical Geology* **256**, 259–268 (2008).
49. Di Matteo, V., Mangiacapra, A., Dingwell, D. B. & Orsi, G. Water solubility and speciation in shoshonitic and latitic melt composition from Campi Flegrei Caldera (Italy). *Chemical Geology* **229**, 113–124 (2006).
50. Botcharnikov, R. E., Koepke, J., Holtz, F., McCammon, C. & Wilke, M. The effect of water activity on the oxidation and structural state of Fe in a ferro-basaltic melt. *Geochimica et Cosmochimica Acta* **69**, 5071–5085 (2005).
51. Benne, D. & Behrens, H. Water solubility in haplobasaltic melts. *ejm* **15**, 803–814 (2003).
52. Berndt, J. *et al.* A combined rapid-quench and H_2 -membrane setup for internally heated pressure vessels: Description and application for water solubility in basaltic melts. *American Mineralogist* **87**, 1717–1726 (2002).
53. Dixon, J. E., Stolper, E. M. & Holloway, J. R. An Experimental Study of Water and Carbon Dioxide Solubilities in Mid-Ocean Ridge Basaltic Liquids. Part I: Calibration and Solubility Models. *Journal of Petrology* **36**, 1607–1631 (1995).
54. Mysen, B. O. Solution mechanisms of silicate in aqueous fluid and H2O in coexisting silicate melts determined in-situ at high pressure and high temperature. *Geochimica et Cosmochimica Acta* **73**, 5748–5763 (2009).
55. Hirose, K., Wood, B. & Vočadlo, L. Light elements in the Earth's core. *Nature Reviews Earth and Environment* **2**, 645–658 (2021).
56. Tsutsumi, Y. *et al.* Origin of Earth's hydrogen and carbon constrained by their core-mantle partitioning and bulk Earth abundance. *Nat Commun* **16**, 10038 (2025).
57. Jiang, Z., He, Y., Zhang, Z., Key Laboratory of Planetary Science and Frontier Technology, Institute of Geology and Geophysics, Chinese Academy of Sciences, Beijing 100029, China, & College of Earth and Planetary Sciences, University of Chinese Academy of Sciences, Beijing 100029,

China. Primordial hydrogen partitioning at Earth's core–mantle boundary: Multicomponent effects revealed by machine learning-augmented first-principles simulations. *Earth and Planetary Physics* **9**, 1001–1009 (2025).
58. Tagawa, S. *et al.* Experimental evidence for hydrogen incorporation into Earth's core. *Nat Commun* **12**, 2588 (2021).
59. Yuan, L. & Steinle-Neumann, G. Strong Sequestration of Hydrogen Into the Earth's Core During Planetary Differentiation. *Geophysical Research Letters* **47**, e2020GL088303 (2020).
60. Malavergne, V. *et al.* Experimental constraints on the fate of H and C during planetary core-mantle differentiation. Implications for the Earth. *Icarus* **321**, 473–485 (2019).
61. Clesi, V. *et al.* Low hydrogen contents in the cores of terrestrial planets. *Sci. Adv.* **4**, e1701876 (2018).
62. Okuchi, T. Hydrogen Partitioning into Molten Iron at High Pressure: Implications for Earth's Core. *Science* **278**, 1781–1784 (1997).
63. Miozzi, F. *et al.* Experiments reveal extreme water generation during planet formation. *Nature* **648**, 551–555 (2025).
64. Wu, J. *et al.* Origin of Earth's Water: Chondritic Inheritance Plus Nebular Ingassing and Storage of Hydrogen in the Core. *JGR Planets* **123**, 2691–2712 (2018).
65. Zhang, Z. *et al.* Free Energies of Fe-O-Si Ternary Liquids at High Temperatures and Pressures: Implications for the Evolution of the Earth's Core Composition. *Geophysical Research Letters* **49**, e2021GL096749 (2022).
66. Takafuji, N., Hirose, K., Mitome, M. & Bando, Y. Solubilities of O and Si in liquid iron in equilibrium with (Mg,Fe)SiO3 perovskite and the light elements in the core. *Geophysical Research Letters* **32**, 1–4 (2005).
67. Hirose, K. *et al.* Hydrogen Limits Carbon in Liquid Iron. *Geophysical Research Letters* **46**, 5190–5197 (2019).
68. Luo, H., Dorn, C. & Deng, J. The interior as the dominant water reservoir in super-Earths and sub-Neptunes. *Nat Astron* **8**, 1399–1407 (2024).
69. Bouhifd, M. A. & Jephcoat, A. P. Convergence of Ni and Co metal–silicate partition coefficients in the deep magma-ocean and coupled silicon–oxygen solubility in iron melts at high pressures. *Earth and Planetary Science Letters* **307**, 341–348 (2011).
70. Fischer, R. A. *et al.* High pressure metal–silicate partitioning of Ni, Co, V, Cr, Si, and O. *Geochimica et Cosmochimica Acta* **167**, 177–194 (2015).
71. Cohen, A. J., Mori-Sánchez, P. & Yang, W. Challenges for density functional theory. *Chem. Rev.* **112**, 289–320 (2012).
72. Grimme, S., Antony, J., Ehrlich, S. & Krieg, H. A consistent and accurate ab initio parametrization of density functional dispersion correction (DFT-D) for the 94 elements H-pu. *J. Chem. Phys.* **132**, 154104 (2010).
73. Smirnov, G. S., Peil, O. E., Ruban, A. V., Simak, S. I. & Belonoshko, A. B. Impact of magnetism on Fe phase diagram under extreme conditions. *Phys. Rev. Materials* **9**, L040601 (2025).
74. Yu, H. *et al.* Spin-dependent graph neural network potential for magnetic materials. *Phys. Rev. B* **109**, 144426 (2024).
75. Furness, J. W., Kaplan, A. D., Ning, J., Perdew, J. P. & Sun, J. Accurate and Numerically Efficient r^2 SCAN Meta-Generalized Gradient Approximation. *J. Phys. Chem. Lett.* **11**, 8208–8215 (2020).
76. Adamo, C. & Barone, V. Toward reliable density functional methods without adjustable

parameters: The PBE0 model. *The Journal of Chemical Physics* **110**, 6158–6170 (1999).
77. Messling, N. *et al.* Ru and W isotope systematics in ocean island basalts reveals core leakage. *Nature* **642**, 376–380 (2025).
78. Corgne, A., Liebske, C., Wood, B. J., Rubie, D. C. & Frost, D. J. Silicate perovskite-melt partitioning of trace elements and geochemical signature of a deep perovskitic reservoir. *Geochimica et Cosmochimica Acta* **69**, 485–496 (2005).
79. Wipperfurth, S. A., Guo, M., Šrámek, O. & McDonough, W. F. Earth's chondritic th/U: Negligible fractionation during accretion, core formation, and crust–mantle differentiation. *Earth and Planetary Science Letters* **498**, 196–202 (2018).
80. Gardner, J. L. A. *et al.* Distillation of atomistic foundation models across architectures and chemical domains. Preprint at https://doi.org/10.48550/arXiv.2506.10956 (2025).
81. Kresse, G. & Furthmüller, J. Efficiency of ab-initio total energy calculations for metals and semiconductors using a plane-wave basis set. *Computational Materials Science* **6**, 15–50 (1996).
82. Kresse, G. & Furthmüller, J. Efficient iterative schemes for *ab initio* total-energy calculations using a plane-wave basis set. *Phys. Rev. B* **54**, 11169–11186 (1996).
83. Blöchl, P. E. Projector augmented-wave method. *Phys. Rev. B* **50**, 17953–17979 (1994).
84. Perdew, J. P. *et al.* Restoring the Density-Gradient Expansion for Exchange in Solids and Surfaces. *Physical Review Letters* **100**, 136406 (2008).
85. Hjorth Larsen, A. *et al.* The atomic simulation environment—a Python library for working with atoms. *Journal of Physics: Condensed Matter* **29**, 273002 (2017).
86. Guillot, B. & Sator, N. Carbon dioxide in silicate melts: A molecular dynamics simulation study. *Geochimica et Cosmochimica Acta* **75**, 1829–1857 (2011).
87. Song, K. *et al.* General-purpose machine-learned potential for 16 elemental metals and their alloys. *Nat Commun* **15**, 10208 (2024).
88. Rzeplinski, I., Sanloup, C., Gilabert, E. & Horlait, D. Hadean isotopic fractionation of xenon retained in deep silicates. *Nature* **606**, 713–717 (2022).
89. Crépisson, C., Blanchard, M., Lazzeri, M., Balan, E. & Sanloup, C. New constraints on Xe incorporation mechanisms in olivine from first-principles calculations. *Geochimica et Cosmochimica Acta* **222**, 146–155 (2018).
90. Paula Leite, R. & De Koning, M. Nonequilibrium free-energy calculations of fluids using LAMMPS. *Computational Materials Science* **159**, 316–326 (2019).
91. Menon, S., Lysogorskiy, Y., Rogal, J. & Drautz, R. Automated free-energy calculation from atomistic simulations. *Phys. Rev. Materials* **5**, 103801 (2021).
92. Paula Leite, R., Freitas, R., Azevedo, R. & De Koning, M. The Uhlenbeck-Ford model: Exact virial coefficients and application as a reference system in fluid-phase free-energy calculations. *The Journal of Chemical Physics* **145**, 194101 (2016).
93. Park, D., Deng, X. & Deng, J. Melting phase relation of seifertite and pyrite-type SiO2 determined by machine learning potentials. Preprint at https://doi.org/10.48550/arXiv.2510.13119 (2025).
94. Andrault, D. *et al.* Comment on: Melting behavior of SiO2 up to 120 GPa (andrault et al. 2020). *Phys Chem Minerals* **49**, 3 (2022).

Supplementary Files

This is a list of supplementary files associated with this preprint. Click to download.

- SupplementaryData.xlsx